

Neural Canonical Transformations for Quantum Anharmonic Solids of Lithium

Qi Zhang¹, Xiaoyang Wang,² Rong Shi,^{3,1} Xinguo Ren^{1,*}, Han Wang^{2,4,†} and Lei Wang^{1,‡}
¹Beijing National Laboratory for Condensed Matter Physics and Institute of Physics, Chinese Academy of Sciences,
 Beijing 100190, China

²Laboratory of Computational Physics, Institute of Applied Physics and Computational Mathematics,
 Fenghao East Road 2, 100094 Beijing, China

³CAS Key Laboratory of Quantum Information, University of Science and Technology of China, Hefei 230026, Anhui, China

⁴HEDPS, CAPT, College of Engineering, Peking University, 100871 Beijing, China

 (Received 26 December 2024; accepted 27 May 2025; published 20 June 2025)

Lithium is a typical quantum solid, characterized by cubic structures at ambient pressure. As the pressure increases, it forms more complex structures and undergoes a metal-to-semiconductor transformation, complicating theoretical and experimental analyses. We employ the neural canonical transformation approach, a variational method based on probabilistic generative models, to investigate the quantum anharmonic effects in lithium solids at finite temperatures. This approach combines a normalizing flow for phonon excited-state wave functions with a probabilistic model for the occupation of energy levels, optimized jointly to minimize the free energy. Our results indicate that quantum anharmonicity lowers the *bcc-fcc* transition temperature compared to classical molecular dynamics predictions. At high pressures, the predicted fractional coordinates of lithium atoms in the *cI16* structure show good quantitative agreement with experimental observations. Finally, contrary to previous beliefs, we find that the poor metallic *oC88* structure is stabilized by the potential energy surface obtained via high-accuracy electronic structure calculations, rather than thermal or quantum effects.

DOI: 10.1103/p3th-25bc

Introduction—Accurate prediction of crystal structures has long been a central focus in materials science. At low temperatures, a deep understanding of the physical properties of crystals composed of light elements typically requires proper treatment of nuclear quantum effects with anharmonicity [1–5]. These effects can play a crucial role in determining the crystal structure, as seen in hydrogen [6–9], helium [10–12], and hydrides [13–16]. In this Letter, we explore one of the most notable examples: lithium, the lightest alkali metal, where the quantum effects of nuclei are pronounced in a wide range of pressures and temperatures [17]. Although lithium behaves as a nearly free-electron metal at low pressure and adopts simple, high-symmetry cubic structures, the free energy difference between its *bcc* (body-centered cubic) and *fcc* (face-centered cubic) structures is less than 1 meV/atom [18–21], making precise calculations challenging. Additionally, lithium exhibits several metastable structures that further complicate experimental measurements [22]. As the pressure increases, lithium exhibits complex physical behaviors, such as anomalous melting curves [17,23,24], and intriguing phase transitions from metal to semiconductor and back [25–27]. Moreover, some

high-pressure phases consist of large unit cells with tens or even hundreds of atoms [27–29], posing substantial challenges for both theoretical and experimental studies.

Numerical approaches to studying quantum crystals at finite temperatures include the well-established path integral molecular dynamics [30] and path integral Monte Carlo [31]. In recent years, inspired by the successful application of vibrational self-consistent field theory in molecular studies [32–34], efforts have been made to extend it to study crystals [2,3,12,18]. However, it relies on a Taylor expansion of the Born-Oppenheimer energy surface (BOES), and the wave function is a simple Hartree product. The stochastic self-consistent harmonic approximation (SSCHA) [5,13,14] provides an alternative by accounting for both ionic quantum and anharmonic effects without assumptions on the specific function form of the BOES. Nevertheless, it still relies on the Gaussian variational density matrices to define the quantum probability distribution. Recent developments have extended SSCHA to non-Gaussian assumptions, yet the entropy is still restricted to Gaussian approximations [35,36].

In this Letter, we utilize the recently developed neural canonical transformations (NCT) approach [37–39], which is a variational density matrix method based on deep generative models, to study quantum lattice dynamics of lithium. NCT constructs orthogonal variational wave functions to describe phonons through a normalizing flow

*Contact author: renxg@iphy.ac.cn

†Contact author: wang_han@iapcm.ac.cn

‡Contact author: wanglei@iphy.ac.cn

model [37–45]. Additionally, we create a probabilistic model to describe the classical energy occupation probabilities for these phonons, allowing for accurate entropy calculations. For electronic calculations, we employ the Deep Potential model [29,46,47], a machine learning BOES, offering significant computational efficiency improvements over density functional theory (DFT) calculations. NCT’s key advantage is its ability to integrate quantum and anharmonic effects of nuclei into the wave functions, which facilitates the determination of the phonon spectrum. Moreover, the independently optimized phonon energy occupation probabilities enable the computation of anharmonic entropy. The NCT codes for lithium are open-sourced and publicly available [48].

The vibrational Hamiltonian of quantum solids—Due to the substantial mass difference between electrons and nuclei, typically spanning several orders of magnitude, the Born-Oppenheimer approximation can be applied to decouple their motions and treat them independently. The vibrational Hamiltonian is expressed as $H_{\text{vib}} = -\sum_i (1/2M)\nabla_i^2 + V_{\text{el}}(\mathbf{R})$, where the mass of a lithium atom is $M = 6.941$ amu. The term $V_{\text{el}}(\mathbf{R})$ is the BOES, derived from electronic structure calculations at nuclear positions \mathbf{R} . In this Letter, to ensure both accuracy and computational efficiency, we use the Deep Potential model to fit the BOES [29,46,47], which is derived from DFT calculations using the Perdew-Burke-Ernzerhof (PBE) functional [50].

The dynamical matrix can be derived from the Hessian of V_{el} at the equilibrium position \mathbf{R}_0 [4,51–55]: $C_{(i\alpha),(j\beta)} = (1/M)[\partial^2 V_{\text{el}}/\partial u_{i\alpha}\partial u_{j\beta}]$, where i, j index the nuclei, α, β represent the Cartesian components, and the displacement coordinates are defined as $\mathbf{u} = \mathbf{R} - \mathbf{R}_0$. Diagonalizing the matrix in a supercell containing N atoms yields $D = 3N - 3$ nonzero eigenvalues, which correspond to the number of phonon modes. The eigenvalues are related to the squares of the phonon frequencies, ω_k^2 ($k = 1, 2, \dots, D$), and the associated eigenvectors define the unitary transformation from displacement coordinates \mathbf{u} to phonon coordinates \mathbf{q} . Consequently, the Hamiltonian can be expressed in phonon coordinates,

$$H_{\text{vib}} = \frac{1}{2} \sum_{k=1}^D \left(-\frac{\partial^2}{\partial q_k^2} + \omega_k^2 q_k^2 \right) + V_{\text{anh}}(\mathbf{q}), \quad (1)$$

where the term V_{anh} represents the anharmonic contributions, as detailed in [55]. In this representation, the separation of high and low-frequency modes greatly enhances the efficiency in the following calculations.

Neural canonical transformation for variational density matrix—The solution for a many-body system in the canonical ensemble can be obtained by minimizing the Helmholtz free energy for a variational density matrix,

$$F = k_B T \text{Tr}(\rho \ln \rho) + \text{Tr}(\rho H_{\text{vib}}), \quad (2)$$

where k_B is the Boltzmann constant and T is the temperature. Assuming that the phonons occupy the states $|\Psi_n\rangle$ with probability p_n , the variational density matrix can be represented in terms of these quantum states as

$$\rho = \sum_n p_n |\Psi_n\rangle \langle \Psi_n|, \quad (3)$$

where $\mathbf{n} = (n_1, n_2, \dots, n_D)$ indexes the energy levels of the phonons. An unbiased estimate of the anharmonic free energy for the variational density matrix Eq. (3) can be written as nested thermal and quantum expectations,

$$F = \mathbb{E}_{\mathbf{n} \sim p_n} \left[k_B T \ln p_n + \mathbb{E}_{\mathbf{q} \sim |\Psi_n(\mathbf{q})|^2} \left[\frac{H_{\text{vib}} \Psi_n(\mathbf{q})}{\Psi_n(\mathbf{q})} \right] \right], \quad (4)$$

where $\Psi_n(\mathbf{q}) = \langle \mathbf{q} | \Psi_n \rangle$ represent the phonon wave functions. The symbol \mathbb{E} is the statistical expectation, which can be estimated through sampling [39,71]. In this Letter, the variational parameters within the energy occupation probabilities and wave functions are denoted as $\boldsymbol{\mu}$ and $\boldsymbol{\theta}$, respectively, i.e., $p_n = p_n(\boldsymbol{\mu})$, $\Psi_n(\mathbf{q}) = \Psi_n(\boldsymbol{\theta}, \mathbf{q})$. These parameters can be optimized via gradient descent [72], with F as the loss function. The gradients $\nabla_{\boldsymbol{\mu}} F$ and $\nabla_{\boldsymbol{\theta}} F$ [55] can be efficiently computed using automatic differentiation [49].

In a supercell with D vibrational modes, setting a cutoff of K energy levels per phonon (i.e., $n_k = 1, 2, \dots, K$) results in an exponentially huge state space of K^D . For supercells containing hundreds of atoms, directly representing the energy occupation probabilities p_n becomes impractical in computations. In the study of lithium, we assume that the probability distributions take a product form [73]: $p_n = \prod_{k=1}^D p(n_k)$, where $p(n_k)$ represents the probability of the k th phonon occupying state n_k , and they are governed by learnable parameters $\boldsymbol{\mu}$. We have checked that an even more powerful variational autoregressive network [38,74,75] does not improve results, likely due to weak coupling between phonon modes. The entropy is the expectation of the probabilities

$$S = \mathbb{E}_{\mathbf{n} \sim p_n} [-k_B \ln p_n]. \quad (5)$$

We note the nonlinear SSCHA [35,36] corresponds to even further simplification of p_n , which assumes that the entropy is given by a set of independent harmonic oscillators.

To construct variational wave functions, we apply a unitary transformation to a set of orthogonal basis states [37–39]: $|\Psi_n\rangle = U_{\boldsymbol{\theta}} |\Phi_n\rangle$, where the basis states $|\Phi_n\rangle$ are chosen as the wave functions of a D -dimensional harmonic oscillator with frequencies ω_k . We implement the unitary transformation $U_{\boldsymbol{\theta}}$ using a normalizing flow [37–45], which establishes a learnable bijection between the phonon

coordinates \mathbf{q} and a set of quasiphonon coordinates ξ . The bijection is represented as a smooth, reversible function $\xi = f_\theta(\mathbf{q})$, where f_θ consists of neural networks with learnable parameters θ , specifically, a real-valued non-volume preserving network [41]. Accordingly, the orthogonal variational wave functions of all energy levels can be formulated as [39,55]

$$\Psi_n(\mathbf{q}) = \Phi_n(f_\theta(\mathbf{q})) \left| \det \left(\frac{\partial f_\theta(\mathbf{q})}{\partial \mathbf{q}} \right) \right|^{1/2}, \quad (6)$$

where $\Phi_n(\xi) = \langle \xi | \Phi_n \rangle$ are basis states. Notably, in the study of lithium, the computation involves about ten million orthogonal states for each training. The Jacobian determinant in Eq. (6) captures phonon interactions and anharmonic effects, enabling a more flexible and accurate representation. This form outperforms the Gaussian-type assumption in SSCHA, yielding significantly better energy and quantum distributions in an anharmonic potential benchmark, as detailed in Supplemental Material (SM) [55]. NCT remains robust when imaginary phonons appear in strong anharmonicity systems (e.g., saddle points of BOES). In such cases, we can choose the corresponding basis states with real-valued frequencies, and the flow model will automatically optimize to find the most suitable wave functions. A detailed derivation of NCT can be found in SM [55] and our previous work [39].

We can extend NCT naturally to the isothermal-isobaric ensemble, where the goal is to minimize the Gibbs free energy at a target pressure P^* , defined as

$$G = F + P^* \Omega, \quad (7)$$

where Ω is the system volume. From the relation $dG = dF + \Omega \sum \sigma_{\alpha\beta} d\varepsilon_{\alpha\beta}$, once the parameters μ and θ have converged under constant volume optimization (i.e., when $dF = 0$), the gradient of the Gibbs free energy to the strain ε depends only on the stress tensor σ . The stress tensor and pressure can be calculated using the virial theorem [51,55,76]. Then, we can optimize the lattice constants \mathbf{a} through the strain tensor $\varepsilon_{\alpha\beta} = \Omega(\sigma_{\alpha\beta} - P^* \delta_{\alpha\beta})$, which is similar to the structure relaxation in other methods [2,5].

*Anharmonic and nuclear quantum effects on stability—*At ambient conditions, lithium adopts a simple *bcc* structure. As the temperature decreases, experiments have demonstrated that the true ground state of lithium is *fcc* [22]. Some calculations have revealed that the free energies of these structures are extremely close [18–21], highlighting the necessity of fully accounting for quantum and anharmonic effects. To investigate the influence of anharmonicity, we first conducted NCT calculations for *bcc* and *fcc* using supercells with 250 and 256 atoms, respectively, at a fixed volume of $19.2 \text{ \AA}^3/\text{atom}$ and temperature 300 K. As a comparative study, we set f_θ in Eq. (6) to an

identity transformation, meaning the phonon wave functions are harmonic oscillators. In this case, only the phonon occupation probabilities p_n in Eq. (4) were optimized.

At a lower temperature of 100 K, the free energies of *fcc* are lower than that of *bcc*, as expected. However, as the temperature increases to 300 K, the impact of anharmonicity becomes evident, as shown in Fig. 1(a). In *fcc*, the free energy difference between the two approaches remains small, about 0.11 meV/atom. In contrast, the anharmonic effects are much stronger in *bcc*, and the difference expands to 2.67 meV/atom. It is also observed that when we only optimized p_n , the free energy of *fcc* is lower than that of *bcc*. However, when the optimization of wave functions is included; i.e., when anharmonic effects are considered, the *bcc* structure becomes more stable. This phenomenon suggests that *bcc* exhibits stronger anharmonicity than *fcc*, underscoring the critical role of anharmonicity in determining the stability.

The findings are further supported by the radial distribution functions (RDF) of nuclei, as shown in Fig. 1(b). The RDF for *fcc* exhibits only slight influence from anharmonic effects. In contrast, the RDF for *bcc* exhibits a smoother curve when anharmonic effects are considered, indicating a reduction in atomic localization. This behavior suggests that anharmonicity softens the system, resulting in a lower zero-point energy (ZPE) than the harmonic approximation. Further insights are provided by the phonon

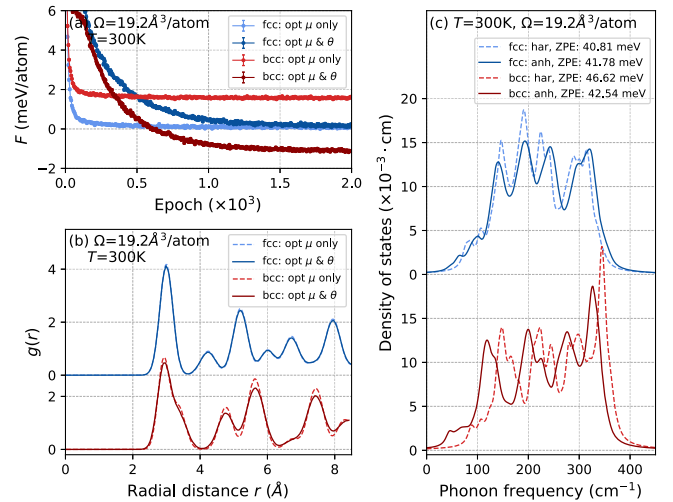


FIG. 1. Numerical results for *fcc* and *bcc* at a fixed volume of $\Omega = 19.2 \text{ \AA}^3/\text{atom}$ and temperature $T = 300 \text{ K}$. (a) Training curves of the Helmholtz free energy $F(\mu, \theta)$ (Eq. (4)). The legend “opt μ only” indicates that only the energy occupation probabilities p_n are optimized, and “opt μ & θ ” means that both p_n and Ψ_n are optimized. (b) Radial distribution functions of nuclei. (c) Phonon density of states per atom. The harmonic (har) frequencies ω_k are calculated from the dynamical matrix, and the anharmonic (anh) frequencies w_k are taken from the single-phonon excitations. The zero-point energies (ZPE) are defined as $E_{\text{ZPE,har}} = \sum_{k=1}^D \omega_k/2N$ and $E_{\text{ZPE,anh}} = \sum_{k=1}^D w_k/2N$.

density of states (DOS) depicted in Fig. 1(c), where the ZPE is determined as half the sum of all phonon frequencies per atom, as detailed in SM [55]. Although the *bcc* structure is more stable at high temperatures, the numerical results reveal that the ZPE of *fcc* remains lower than that of *bcc*. This phenomenon can be explained by the differences in coordination numbers: the coordination number of *bcc* is 8, while that of *fcc* is 12. Hence, atoms in *bcc* interact less strongly with their neighbors, leading to higher quantum fluctuations and greater anharmonicity.

To gain deeper insight into the influence of nuclear quantum effects, we performed calculations on the *bcc* and *fcc* structures under constant pressure. The Gibbs free energies of both structures are extremely close [18–21]. An error of just 1 meV could lead to a shift of more than 100 K in the transition temperature [20]. Figure 2(a) shows the Gibbs free energy difference between these structures at 1 GPa, with the *fcc* structure used as the reference. The two curves intersect at 142 K, indicating a phase transition at this temperature. We also calculated the transition temperature through classical molecular dynamics (MD) simulations with thermodynamic integration on the same BOES, obtaining a value of 185 K. The main difference between these methods is that NCT accounts for the quantum effects, while MD simulations do not. Similar results are also observed at 0 and 2 GPa, as detailed in SM [55], where NCT consistently predicts lower transition temperatures compared to MD.

The ionic entropy of both structures is shown in Fig. 2(b). The anharmonic entropy obtained from NCT is derived directly from the probabilities of energy occupations in Eq. (5), beyond the harmonic oscillator assumption. The entropy of *fcc* is higher than that of the

bcc under the harmonic oscillator assumption. However, when the anharmonicity is considered, the relationship is reversed. The higher entropy of the *bcc* structure is a key factor contributing to its stability in finite temperatures [18,21,53,54,77]. Furthermore, we quantified the free energy difference arising from the anharmonic effects of entropy as $-k_B T(S_{\text{anh}} - S_{\text{har}})$ [inset of Fig. 2(b)], estimating it to be on the order of several meV. This underscores the critical importance of accurately incorporating anharmonic effect in the calculations.

High-pressure structural stability of lithium—Under high pressure, lithium exhibits more complex structures and larger unit cell sizes. We first applied the NCT method to calculate the *cI16* (cubic I-centered, *I-43d*) structure at 100 K, using a supercell of 432 atoms under various pressures. The NCT method optimizes the atom positions through coordinate transformations. Subsequently, we quenched the sampled structures to their ground state with the BOES and analyzed the fractional coordinates (x, x, x) of Wyckoff position *16c* as a function of atomic volume. As depicted in Fig. 3(a), our results are consistent with the experiment reported in Ref. [78], demonstrating the reliability of NCT in structure optimizations.

As illustrated in Fig. 3(b), the phonon DOS and ZPE of the *cI16* and *oC88* (orthorhombic C-face centered, *C2mb*) structures are calculated at 70 GPa. Under the harmonic approximation, the ZPE of both structures are found to be comparable, consistent with the results obtained using the finite displacement and density functional perturbation theory methods [29]. The anharmonic effects soften the phonon spectrum of *cI16*, reducing the ZPE by 4.92 meV and further enhancing its stability. In contrast, the ZPE of *oC88* decreases by only 1.67 meV under anharmonic effects, indicating a smaller impact compared to *cI16*. This result suggests that when the anharmonic effect is considered, the stability of *oC88* decreases, contrary to the expectations of previous studies [26,27,29].

Additionally, we calculated the Gibbs free energies at 100 K, as shown in Fig. 3(c). The free energy of *oC88* remains consistently higher than that of *cI16* across all pressures, which contradicts previous experiments. It has been reported that the resistivity increases sharply by more than 4 orders of magnitude after the *cI16* phase, ultimately transforming into a semiconductor. Compression experiments in Ref. [17] observed the *cI16*-*oC88* transition, as evidenced by changes in crystal color and diffraction patterns. Raman spectra measurements in Ref. [28] detected signals corresponding to the *oC88* phase. Another experiment [24] also observed a phase transition around 60 GPa through the changes in diffraction peaks.

After the *oC88* structure was experimentally observed [17], theoretical studies attempted to explain its stability. However, Ref. [27] concluded from their zero-temperature calculations that *oC88* was only the second most stable phase, with an enthalpy about 1 meV higher than *cI16*,

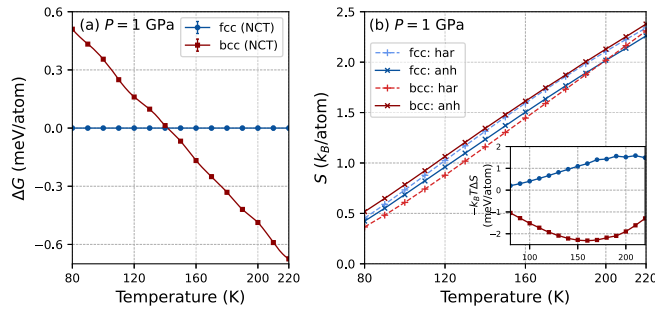


FIG. 2. (a) Gibbs free energy (Eq. (7)) difference between *fcc* and *bcc* at $P = 1$ GPa, using *fcc* as the reference. The error bars represent statistical uncertainties, which are smaller than the data points. For additional sources of uncertainty, refer to [55]. (b) Anharmonic effects on ionic entropy. The anharmonic (anh) entropy is directly obtained from the expectation of the probability distribution (Eq. (5)), while the harmonic (har) entropy is calculated from the harmonic frequencies using $S = \sum_k \{(\omega_k/k_B T)[1/e^{\omega_k/k_B T} - 1] - \ln(1 - e^{-\omega_k/k_B T})\}$. The x axis of the inset represents the temperature, and the y axis corresponds to $-k_B T(S_{\text{anh}} - S_{\text{har}})$ in units of meV/atom.

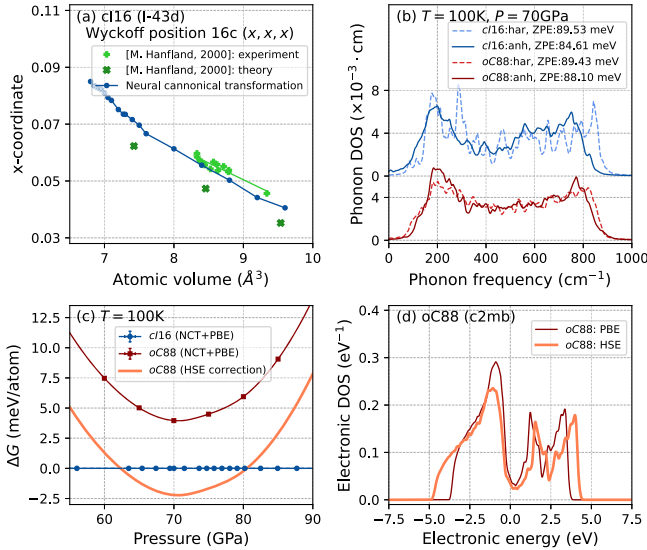


FIG. 3. (a) Fractional coordinates of the Wyckoff position 16c in the *cI16* (*I-43d*) structure. Experimental values are taken from Ref. [78]. (b) Phonon density of states (DOS). (c) Gibbs free energy difference between *cI16* and *oC88* at $T = 100\text{K}$, with *cI16* taken as the reference. The thick orange line indicates the single-point correction using the HSE functional at 70 GPa. (d) Electronic DOS for *oC88* with PBE and HSE functionals.

attributing this to an insufficient consideration of ZPE and thermal effects. In another work [26], the authors also failed to identify *oC88* as a stable structure. In contrast, Ref. [28] found that *oC88* is stable when using the PBE functional with a harmonic ZPE at 200 K. However, a recent study [29] demonstrated that neither harmonic nor anharmonic approximations could reproduce the results of Ref. [28] at various conditions, showing a free energy difference at least 1 meV with *oC88* consistently higher than *cI16*. Surprisingly, as NCT captures nuclear quantum effects and anharmonic behaviors more accurately, the difference increases to 4 meV. It has been observed that DFT often over-stabilizes metallic states relative to non-metallic states [79,80]. Therefore, we strongly suspect that the instability of *oC88* arises from the limited accuracy of the DFT (PBE) calculations used in fitting the BOES [29].

To validate our hypothesis, we employed the NCT-optimized structures at 70 GPa and conducted single-point electronic structure calculations using the high-accuracy Heyd-Scuseria-Ernzerhof (HSE06) functional [51]. The HSE functional incorporates a hybrid exchange-correlation correction, enabling a clearer distinction between metallic and non-metallic states. Notably, HSE calculations are significantly more computationally demanding, requiring approximately 2 orders of magnitude more computational resources than PBE. Additional details of HSE are provided in SM [55]. Our results reveal that the

relative energy of *oC88* compared to *cI16* decreases by 6.17 meV under HSE in comparison to PBE. This reduction is significantly larger than the contributions from ZPE, anharmonic, and finite temperature effects. The HSE correction, depicted as the thick line in Fig. 3(c), predicts a *cI16*-*oC88* phase transition at approximately 62 GPa and 100 K. This finding is consistent with experimental observations, which report a narrow stability range for the *oC88* phase, existing between 62 and 70 GPa, flanked by the *cI16* and *oC40* phases on either side, respectively [17]. The electronic DOS of *oC88*, depicted in Fig. 3(d), shows that while the HSE correction lowers the potential energy, *oC88* still behaves as a poor metal.

Conclusions—In summary, we developed the NCT method [37–39] to study anharmonic quantum solids and applied it to lithium. It enables the calculation of excited-state wave functions of nuclear motions beyond the harmonic approximation, allowing for the extraction of anharmonic phonon spectra. The independently optimized phonon occupation probabilities facilitate the computation of anharmonic entropy. The results demonstrate that quantum anharmonic effects play a crucial role in structural stability and introduce significant corrections to the *fcc-bcc* transition temperature. The fractional coordinates of the *cI16* structure have been determined and closely align with experimental findings. Moreover, we identified that the failure of previous numerical studies [26,27,29] to observe the stability of *oC88* was due to the limitations of the PBE functional in accurately describing poor metallic states. To address this, we applied the HSE functional to refine the results and estimate the stability region of *oC88*. Looking ahead, both experimental and computational investigations suggest that the emergence of novel high-density lithium solid structures between the *cI16* and liquid phases presents a promising avenue for future exploration [24,29]. Overall, NCT shows significant potential for investigating other light-element systems, such as hydrogen [6–9], helium [10–12], and hydride solids [13–16], as well as molecular systems like aspirin and paracetamol [81], where quantum anharmonicity plays a crucial role. Similar to the techniques used in SSCHA [13], NCT could also be extended to calculate electron-phonon coupling, which is important for studying superconductivity. It could greatly enhance our understanding and address a wide range of challenges in quantum crystals.

Acknowledgments—We are grateful for the valuable discussions with Hao Xie, Jian Lv, Xinyang Dong, Zhendong Cao, Zihang Li, Ruisi Wang, and Peize Lin. Some calculations have been done on the supercomputing system in the Huairou Materials Genome Platform. This work is supported by the National Natural Science Foundation of China under Grants No. 92270107, No. T2225018, No. 12188101, No. T2121001,

No. 12134012, and No. 12374067, and the Strategic Priority Research Program of the Chinese Academy of Sciences under Grants No. XDB0500200 and No. XDB30000000.

Data availability—The data that support the findings of this article are openly available [48].

-
- [1] C. Cazorla and J. Boronat, *Rev. Mod. Phys.* **89**, 035003 (2017).
- [2] B. Monserrat, N. D. Drummond, and R. J. Needs, *Phys. Rev. B* **87**, 144302 (2013).
- [3] V. Kapil, E. Engel, M. Rossi, and M. Ceriotti, *J. Chem. Theory Comput.* **15**, 5845 (2019).
- [4] J. A. Flores-Livas, L. Boeri, A. Sanna, G. Profeta, R. Arita, and M. Eremets, *Phys. Rep.* **856**, 1 (2020).
- [5] L. Monacelli, R. Bianco, M. Cherubini, M. Calandra, I. Errea, and F. Mauri, *J. Phys. Condens. Matter* **33**, 363001 (2021).
- [6] S. Azadi, B. Monserrat, W. M. C. Foulkes, and R. J. Needs, *Phys. Rev. Lett.* **112**, 165501 (2014).
- [7] M. Borinaga, I. Errea, M. Calandra, F. Mauri, and A. Bergara, *Phys. Rev. B* **93**, 174308 (2016).
- [8] L. Monacelli, I. Errea, M. Calandra, and F. Mauri, *Nat. Phys.* **17**, 63 (2021).
- [9] L. Monacelli, M. Casula, K. Nakano, S. Sorella, and F. Mauri, *Nat. Phys.* **19**, 845 (2023).
- [10] F. Pederiva and G. V. Chester, *J. Low Temp. Phys.* **113**, 741 (1998).
- [11] E. Vitali, M. Rossi, L. Reatto, and D. E. Galli, *Phys. Rev. B* **82**, 174510 (2010).
- [12] B. Monserrat, N. D. Drummond, C. J. Pickard, and R. J. Needs, *Phys. Rev. Lett.* **112**, 055504 (2014).
- [13] I. Errea, M. Calandra, and F. Mauri, *Phys. Rev. Lett.* **111**, 177002 (2013).
- [14] I. Errea, M. Calandra, and F. Mauri, *Phys. Rev. B* **89**, 064302 (2014).
- [15] I. Errea, M. Calandra, C. J. Pickard, J. R. Nelson, R. J. Needs, Y. Li, H. Liu, Y. Zhang, Y. Ma, and F. Mauri, *Nature (London)* **532**, 81 (2016).
- [16] I. Errea, F. Belli, L. Monacelli, A. Sanna, T. Koretsune, T. Tadano, R. Bianco, M. Calandra, R. Arita, F. Mauri *et al.*, *Nature (London)* **578**, 66 (2020).
- [17] C. L. Guillaume, E. Gregoryanz, O. Degtyareva, M. I. McMahon, M. Hanfland, S. Evans, M. Guthrie, S. V. Sinogeikin, and H. Mao, *Nat. Phys.* **7**, 211 (2011).
- [18] M. Hutcheon and R. Needs, *Phys. Rev. B* **99**, 014111 (2019).
- [19] P. Jerabek, A. Burrows, and P. Schwerdtfeger, *Chem. Commun. (Cambridge)* **58**, 13369 (2022).
- [20] D. M. Riffe and J. D. Christensen, *Phys. Rev. B* **110**, 174109 (2024).
- [21] M. K. Phuthi, Y. Huang, M. Widom, and V. Viswanathan, *arXiv:2406.15491*.
- [22] G. J. Ackland, M. Dunuwille, M. Martinez-Canales, I. Loa, R. Zhang, S. Sinogeikin, W. Cai, and S. Deemyad, *Science* **356**, 1254 (2017).
- [23] A. M. J. Schaeffer, W. B. Talmadge, S. R. Temple, and S. Deemyad, *Phys. Rev. Lett.* **109**, 185702 (2012).
- [24] M. Frost, J. B. Kim, E. E. McBride, J. R. Peterson, J. S. Smith, P. Sun, and S. H. Glenzer, *Phys. Rev. Lett.* **123**, 065701 (2019).
- [25] T. Matsuoka and K. Shimizu, *Nature (London)* **458**, 186 (2009).
- [26] J. Lv, Y. Wang, L. Zhu, and Y. Ma, *Phys. Rev. Lett.* **106**, 015503 (2011).
- [27] M. Marqués, M. I. McMahon, E. Gregoryanz, M. Hanfland, C. L. Guillaume, C. J. Pickard, G. J. Ackland, and R. J. Nelmes, *Phys. Rev. Lett.* **106**, 095502 (2011).
- [28] F. A. Gorelli, S. F. Elatresh, C. L. Guillaume, M. Marqués, G. J. Ackland, M. Santoro, S. A. Bonev, and E. Gregoryanz, *Phys. Rev. Lett.* **108**, 055501 (2012).
- [29] X. Wang, Z. Wang, P. Gao, C. Zhang, J. Lv, H. Wang, H. Liu, Y. Wang, and Y. Ma, *Nat. Commun.* **14**, 2924 (2023).
- [30] G. J. Martyna, A. Hughes, and M. E. Tuckerman, *J. Chem. Phys.* **110**, 3275 (1999).
- [31] J. A. Barker, *J. Chem. Phys.* **70**, 2914 (1979).
- [32] J. M. Bowman, *J. Chem. Phys.* **68**, 608 (1978).
- [33] J. M. Bowman, *Acc. Chem. Res.* **19**, 202 (1986).
- [34] R. Gerber and M. Ratner, *Chem. Phys. Lett.* **68**, 195 (1979).
- [35] A. Siciliano, L. Monacelli, and F. Mauri, *Phys. Rev. B* **110**, 134111 (2024).
- [36] L. Monacelli, A. Siciliano, and N. Marzari, *arXiv:2410.08882*.
- [37] H. Xie, L. Zhang, and L. Wang, *J. Mach. Learn. Res.* **1**, 38 (2022).
- [38] H. Xie, L. Zhang, and L. Wang, *SciPost Phys.* **14** (2023).
- [39] Q. Zhang, R.-S. Wang, and L. Wang, *J. Chem. Phys.* **161**, 024103 (2024).
- [40] L. Dinh, D. Krueger, and Y. Bengio, *arXiv:1410.8516*.
- [41] L. Dinh, J. Sohl-Dickstein, and S. Bengio, *arXiv:1605.08803*.
- [42] L. Wang, Generative models for physicists (2018), <http://wangleiphy.github.io/lectures/PILTutorial.pdf>.
- [43] G. Papamakarios, *arXiv:1910.13233*.
- [44] G. Papamakarios, E. Nalisnick, D. J. Rezende, S. Mohamed, and B. Lakshminarayanan, *J. Mach. Learn. Res.* **22**, 1 (2021), <http://jmlr.org/papers/v22/19-1028.html>.
- [45] Y. Saleh, A. F. Corral, A. Iske, J. Küpper, and A. Yachmenev, *J. Chem. Theory Comput.* **21**, 5221 (2025).
- [46] H. Wang, L. Zhang, J. Han, and W. E, *Comput. Phys. Commun.* **228**, 178 (2018).
- [47] J. Zeng *et al.*, *J. Chem. Phys.* **159**, 054801 (2023).
- [48] The code of neural canonical transformations for lithium solids, implemented with the PYTHON package JAX [49], is available at <https://github.com/zhangqi94/lithium>.
- [49] J. Bradbury, R. Frostig, P. Hawkins, M. J. Johnson, C. Leary, D. Maclaurin, G. Necula, A. Paszke, J. VanderPlas, S. Wanderman-Milne, and Q. Zhang, JAX: Composable transformations of PYTHON + NumPy programs (2018), <https://github.com/jax-ml/jax>.
- [50] J. P. Perdew, K. Burke, and M. Ernzerhof, *Phys. Rev. Lett.* **77**, 3865 (1996).
- [51] R. M. Martin, *Electronic Structure: Basic Theory and Practical Methods* (Cambridge University Press, Cambridge, England, 2020).
- [52] S. Baroni, S. de Gironcoli, A. Dal Corso, and P. Giannozzi, *Rev. Mod. Phys.* **73**, 515 (2001).
- [53] P. Souvatzis, O. Eriksson, M. I. Katsnelson, and S. P. Rudin, *Phys. Rev. Lett.* **100**, 095901 (2008).

- [54] P. Souvatzis, O. Eriksson, M. Katsnelson, and S. Rudin, *Comput. Mater. Sci.* **44**, 888 (2009).
- [55] See Supplemental Material at <http://link.aps.org/supplemental/10.1103/p3th-25bc> for details of the neural canonical transformation approach and additional results, which includes Refs. [56–70].
- [56] C. S. Barrett, *Phys. Rev.* **72**, 245 (1947).
- [57] C. Rao and K. Rao, *Prog. Solid State Chem.* **4**, 131 (1967).
- [58] M. Eger and E. Gross, *Ann. Phys. (N.Y.)* **24**, 63 (1963).
- [59] F. Eger and E. Gross, *Nuovo Cimento (1955–1965)* **34**, 1225 (1964).
- [60] B. S. DeWitt, *Phys. Rev.* **85**, 653 (1952).
- [61] M. Hutchinson, *Commun. Stat.—Simul. Comput.* **18**, 1059 (1989).
- [62] S. S. Schoenholz and E. D. Cubuk, in *Neural Information Processing Systems 33, Vancouver*, edited by H. Larochelle, M. Ranzato, R. Hadsell, M. F. Balcan, and H. Lin (Curran Associates, Inc., New York, 2020), Vol. 33.
- [63] G. Kresse and J. Furthmüller, *Phys. Rev. B* **54**, 11169 (1996).
- [64] Atomic-orbital Based Ab-initio Computation at USTC (ABACUS) is an open-source package for density functional theory calculations. More information can be found at <https://abacus.ustc.edu.cn/main.htm>.
- [65] D. R. Hamann, *Phys. Rev. B* **88**, 085117 (2013).
- [66] Optimized Norm-Conserving Vanderbilt Pseudopotential (ONCVSP) code is available at <http://www.mat-simresearch.com>.
- [67] Fritz Haber Institute *ab initio* materials simulations (FHI-aims) is a quantum mechanics software package based on numeric atom-centered orbitals. More information can be found at <https://fhi-aims.org>.
- [68] V. Blum, R. Gehrke, F. Hanke, P. Havu, V. Havu, X. Ren, K. Reuter, and M. Scheffler, *Comput. Phys. Commun.* **180**, 2175 (2009).
- [69] J. Heyd, G. E. Scuseria, and M. Ernzerhof, *J. Chem. Phys.* **118**, 8207 (2003).
- [70] K. He, X. Zhang, S. Ren, and J. Sun, in *Proceedings of the IEEE Conference on Computer Vision and Pattern Recognition (CVPR)* (2016).
- [71] F. Becca and S. Sorella, *Quantum Monte Carlo Approaches for Correlated Systems* (Cambridge University Press, Cambridge, England, 2017).
- [72] D. P. Kingma and J. Ba, [arXiv:1412.6980](https://arxiv.org/abs/1412.6980).
- [73] J. Martyn and B. Swingle, *Phys. Rev. A* **100**, 032107 (2019).
- [74] D. Wu, L. Wang, and P. Zhang, *Phys. Rev. Lett.* **122**, 080602 (2019).
- [75] J.-G. Liu, L. Mao, P. Zhang, and L. Wang, *Mach. Learn.* **2**, 025011 (2021).
- [76] O. H. Nielsen and R. M. Martin, *Phys. Rev. B* **32**, 3780 (1985).
- [77] P. Söderlind, B. Grabowski, L. Yang, A. Landa, T. Björkman, P. Souvatzis, and O. Eriksson, *Phys. Rev. B* **85**, 060301(R) (2012).
- [78] M. Hanfland, K. Syassen, N. Christensen, and D. Novikov, *Nature (London)* **408**, 174 (2000).
- [79] Y. Ma, M. Eremets, A. R. Oganov, Y. Xie, I. Trojan, S. Medvedev, A. O. Lyakhov, M. Valle, and V. Prakapenka, *Nature (London)* **458**, 182 (2009).
- [80] Y. Ma, A. R. Oganov, and C. W. Glass, *Phys. Rev. B* **76**, 064101 (2007).
- [81] H. E. Sauceda, V. Vassilev-Galindo, S. Chmiela, K.-R. Müller, and A. Tkatchenko, *Nat. Commun.* **12**, 442 (2021).